Stress-induced permeability evolution in a quasi-brittle geomaterial

T. J. Massart[1,2] and A. P. S. Selvadurai[3]

Received 21 February 2012; revised 23 May 2012; accepted 31 May 2012; published 20 July 2012.

[1] This paper presents the application of a computational homogenization technique to examine the stress-induced permeability evolution in a quasi-brittle material susceptible to damage. The concepts involved in the constitutive modeling and the computational procedures are summarized. The developments are applied to investigate the response of the model in simulating experimental investigations of permeability evolution in a granitic rock. The influence of both the isotropic and the deviatoric stress states on the evolution of the spatially averaged permeability is derived from the computational simulations and is compared with experimental observations. It is shown that with the provision of supplemental material parameters the computational approach is able to satisfactorily match the experimental results.

Citation: Massart, T. J., and A. P. S. Selvadurai (2012), Stress-induced permeability evolution in a quasi-brittle geomaterial, *J. Geophys. Res.*, *117*, B07207, doi:10.1029/2012JB009251.

1. Introduction

[2] The mechanical behavior of fluid-saturated porous media constitutes an important development in the study of geomaterials. The classical theory of poroelasticity due to *Biot* [1941] takes into account the mechanics of coupling between the porous fabric and the fluid saturating the pore space. It has been successfully applied to many areas of engineering geosciences ranging from the study of soil consolidation to the examination of factors that can contribute to earthquake phenomena. The literature in this area is extensive and no attempt will be made to provide a comprehensive review. The review articles and volumes by *Scheidegger* [1960], *Paria* [1963], *Rice and Cleary* [1976], *Detournay and Cheng* [1993], *Selvadurai* [1996, 2007], *Coussy* [1995] and *Schanz* [2009] can be consulted for accounts of recent developments. A fundamental assumption in the theory proposed by *Biot* [1941] is that the material properties remain unchanged during the coupled interaction between the porous skeleton and the saturating fluid; properties such as the porosity, deformability and permeability are assumed to remain unchanged even though the fabric of the porous medium itself can experience change. In modern environmental geomechanics it becomes necessary to consider the alterations in the properties of the porous medium resulting from actions at various scales of interest. For example, the porous fabric can experience micro-mechanical damage due to transport of reactive fluids that can lead to changes in the deformability, strength and permeability characteristics. By far the most common action that can alter the properties of the porous medium is the micromechanical damage resulting from the application of stresses. Experimental results of *Zoback and Byerlee* [1975], *Shiping et al.* [1994] and *Kiyama et al.* [1996] conducted on granite and limestone indicate variations in permeability with an increase in deviatoric stress states. Results presented by *Souley et al.* [2001] also point to alterations in the permeability of the porous medium at stress states well below the peak failure loads. The micro-mechanical damage that contributes to the alteration in the permeability in particular has important implications for poromechanical applications including the development of fracture in fluid-saturated materials [*Mahyari and Selvadurai*, 1998; *Selvadurai*, 2004; *Selvadurai and Shirazi*, 2005]. In particular, the duration of transient processes involving pore fluid pressure dissipation can be influenced by the changes in permeability. There are two options that can be adopted to account for stress-induced alteration in the permeability: either (i) conduct physical experiments to capture all modes of permeability evolution with stress, leading to experimentally derived relationships that are state-space representations of permeability with appropriate stress invariants, which can also account for permeability reduction/increase with isotropic compression [e.g., *Zhu and Wong*, 1997; *Selvadurai and Glowacki*, 2008; *Zhu et al.*, 2007; *Selvadurai et al.*, 2011] or (ii) develop a computational approach for examining permeability evolution, taking into consideration the micromechanical processes that contribute to permeability evolution; these can include local fabric heterogeneity of geomaterials, the interface phenomena between heterogeneous domains, including slip, separation

[1]Building, Architecture and Town Planning Department (BATir), Université Libre de Bruxelles (ULB), Brussels, Belgium.
[2]On leave at Department of Civil Engineering and Applied Mechanics, McGill University, Montreal, Canada.
[3]Department of Civil Engineering and Applied Mechanics, McGill University, Montreal, Canada.

Corresponding author: T. J. Massart, Building, Architecture and Town Planning Department (BATir), Université Libre de Bruxelles (ULB), Av. F.-D. Roosevelt 50, BE-1050 Brussels, Belgium. (thmassar@batir.ulb.ac.be)

0148-0227/12/2012JB009251

and locking, intra-domain brittle fracture and damage development in the form of inter-granular micro-cracking of the heterogeneous fabric itself. The former approach is the most straightforward but requires access to sophisticated experimental techniques that can examine both the evolution of permeability and its anisotropy. The second approach is both modeling and input parameter intensive but merits further investigation in view of the possible development of an approach that can supplement or confirm experimental results. Several investigators have applied damage mechanics concepts to examine the evolution of permeability of rocks and examples of such studies, including references to further works, are given by *Shao et al.* [1999], *Zhou et al.* [2006], and *Hu et al.* [2010].

[3] In this paper we present a computational approach for investigating permeability evolution in a heterogeneous porous medium. A three-dimensional Voronoi tessellation technique is used to idealize the geomaterial with a heterogeneous fabric. A computational homogenization technique is used to examine the fabric; the interface mechanical behavior is modeled by a Coulomb failure condition with a tension cut-off and the damage evolution law, based on a cohesive crack model, incorporates measurable micromechanical parameters including the tensile strength, cohesion, the Mode-I tensile fracture energy and the interface stiffness parameters that can be related to the elasticity characteristics of the grain. The details of the computational procedures are summarized in the paper. The procedures are used to estimate the variation of permeability of the heterogeneous fabric with confining pressure and deviator stress applied in triaxial testing and the developments are compared with experimental results for the permeability evolution in granite samples.

2. Fine-Scale Modeling

2.1. Failure Modeling

[4] Modeling failure in quasi-brittle materials using continuum descriptions requires the use of constitutive laws that can account for softening. This results in complex computations, potentially requiring advanced path-tracking techniques [*Geers*, 1999] when the post-peak response has to be traced. In mathematical terms, the use of softening laws in continuum descriptions is known to result in the loss of the ellipticity of the partial differential equations of the equilibrium problem, and the loss of well-posedness of the corresponding boundary value problem. In computational modeling exercises, this results in a pathological mesh dependency of the results [*Peerlings et al.*, 1996], with an unrealistic increase in the brittleness of the fracture process that depends upon discretization refinement. Various regularization remedies have been proposed to restore the well-posedness of the equilibrium problem; these range from the introduction of non-locality in the constitutive response [*Peerlings et al.*, 1996] to the introduction of cohesive crack models within a non-localizing matrix, both at predefined locations [*Lotfi and Shing*, 1994] or using so-called XFEM enrichments [*Wells and Sluys*, 2001].

[5] To capture the influence of cracking, a trade-off between accuracy and computational efficiency is necessary. Continuum-based non-local descriptions are generally computing intensive because fine mesh refinement is required in the potential localization zones. Consequently, in this research, the process of cracking is incorporated by means of cohesive laws in a priori positioned interface elements. Note that this choice is physically consistent with discrete orientation-based approaches [*Hu et al.*, 2010], with the difference here being that spatial connectivity and cracking is explicitly modeled. The remainder of the material is discretized with linear elastic elements. This is motivated by the existing fabric of the material; the polycrystalline rock joints can be represented using this discretization technique. To minimize the computational effort, the attention will be restricted to a priori positioned potential cracks at the grain boundaries of the polycrystalline rock. Subgrain cracking, fragmentation and crushing will not be included in this contribution, yet developing the upscaling relations (see Section 3) in a flexible manner will allow the potential incorporation of grain cracking and crushing in future developments. Conversely, this technique can also be used to represent crack development within geomaterials with cemented zones between grains. In the latter case, sufficient randomness in the incorporation of potential cracks in a medium is required to avoid any bias in the anisotropic degradation patterns obtained. As will be demonstrated in Section 5, this choice, therefore, requires verifying the ability of the Representative Volume Element (RVE) to produce general cracking schemes.

[6] In order to restrict as much as possible the number of fine-scale material parameters, and since the main focus of this approach is on the stiffness degradation, a 3D scalar damage model with an exponential evolution law will be considered for the potential cracks. This law links the traction vector $\vec{T}$ across the interface to the relative displacement vector $\vec{\delta}$

$$\vec{T} = (1 - D)\mathbf{H} \cdot \vec{\delta} \tag{1}$$

where D is a scalar damage variable that increases from zero (virgin material) to unity (complete failure). Note that for the behavior of potential cracks, the use of (1) implicitly introduces the simplifying assumptions that no pre-peak dissipation is present, that no stiffness recovery is considered under cyclic loading, and that the normal and tangential stiffnesses are degraded at the same rate. Also note that the use of (1) requires the implicit assumption that only the cracking evolution is examined, without accounting for the presence of potential initial cracks. In (1), $\mathbf{H}$ is a 3D elastic stiffness (second-order tensor) that depends on the normal and tangential elastic stiffnesses k_n and k_t of the cohesive zone

$$[\mathbf{H}] = diag(k_t, k_t, k_n) \tag{2}$$

Such elastic parameters of the cohesive zone can be obtained from properties of rock joints, or from the bulk elastic properties if an initially homogeneous material is assumed. The latter assumption will be used in the present contribution. To allow reproducing macroscopically the rock elastic properties with the presence of thin joints, the elastic properties of the interface elements will be deduced as

$$\sigma = \frac{E}{h}\underbrace{h\varepsilon}_{\delta_n} = k_n\delta_n; \quad \tau_t = \frac{G}{h}\underbrace{h\gamma_t}_{\delta_t} = k_t\delta_t; \quad \tau_s = \frac{G}{h}\underbrace{h\gamma_s}_{\delta_s} = k_t\delta_s \tag{3}$$

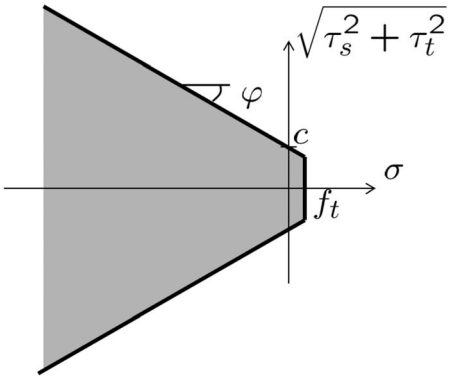

Figure 1. Damage criterion used for the cohesive zones expressed in the stress space.

where E and G are the bulk properties, and h is an assumed thickness of the cracking zone (cemented zone between grains for instance). This operation could theoretically be avoided by the introduction of the cohesive response at damage initiation by resorting to XFEM approaches based on *partition of unity concepts*, see [*Wells and Sluys*, 2001]. However, such formulations are difficult to implement, especially when multiple cracks have to be considered simultaneously.

[7] In order to account for the different behaviors in tension and compression, a damage threshold consisting of a Mohr-Coulomb criterion with tension cut-off is considered as illustrated in Figure 1 in the space of stress components of the cohesive zone. For the purpose of its implementation in a damage mechanics setting, it is translated in the space of relative displacement components of the cohesive zone. The damage-controlling parameter κ is therefore taken as the most critical value of an equivalent relative displacement defined by

$$\delta_{eq} = \max\left\{\frac{f_t}{c}(\tan\varphi)\delta_n + \frac{f_t}{c}\frac{k_t}{k_n}\sqrt{\delta_s^2 + \delta_t^2}, \quad \delta_n\right\} \tag{4}$$

where δ_n and $\sqrt{\delta_s^2 + \delta_t^2}$ are the magnitudes of the normal and tangential relative displacements, respectively; f_t is the tensile strength, c is the cohesion, and φ is the angle of friction. Note that the use of this criterion implicitly introduces the assumption that the frictional behavior of the crack is constant during sliding. The damage evolution law for the cohesive crack is given by *Mercatoris and Massart* [2011], allowing exponential decay of the stress across the cohesive zone to be accounted for in mode I loading:

$$D(\kappa) = 1 - \frac{f_t}{k_n \kappa} e^{-\frac{f_t}{G_{f,I}}\left(\kappa - \frac{f_t}{k_n}\right)} \quad \text{for} \quad \kappa \geq \frac{f_t}{k_n} \tag{5}$$

where $G_{f,I}$ is the mode-I tensile fracture energy. In the present formulation using relationship (4), the strength properties (f_t, c) and the mode-I fracture energy $G_{f,I}$ implicitly define the energy dissipation under pure shear which is given by

$$G_{f,II} = \left(\frac{c}{f_t}\right)^2 \left(\frac{k_n}{k_t}\right) G_{f,I} \tag{6}$$

The detailed developments leading to relationships (4) to (6) are reported in Appendix A.

2.2. Transport Modeling in a Damaged Medium

[8] The objective of the paper is to assess the ability of computational homogenization techniques to reproduce the effective permeability increases observed in experiments, using the same discretization as in the mechanical problem, i.e. the matrix material will be modeled with 3D elements with fixed permeability, whereas the potential cracks will be represented by interface elements, with variable permeability. As in *Souley et al.* [2001], *Zhou et al.* [2006], and *Jiang et al.* [2010], a unilateral coupling will be assumed, i.e. the local permeability properties of potential cracks will be dependent on the actual damage state deduced from mechanical actions. For each equilibrium configuration obtained from the mechanical simulation, a modified Darcy assumption will be used as

$$\vec{q}_m = -\frac{\mathbf{K}(D)}{\mu}\vec{\nabla}_m p \tag{7}$$

where the local permeability tensor $\mathbf{K}$ of points of the interface elements depends on their (fixed) damage state D, p is the fluid pressure, μ is the dynamic viscosity and $\vec{\nabla}_m$ is the gradient operator. Hydraulically, the interface is considered to be planar and isotropic (i.e. diagonal local permeability tensor). The transport problem within the RVE therefore reads

$$\vec{\nabla}_m \cdot \left(-\frac{\mathbf{K}(D)}{\mu}\vec{\nabla}_m p\right) = 0 \tag{8}$$

In interface elements, the pressure gradients used in the formulation are defined as follows: the normal pressure gradient is taken as the pressure jump between two nodes of the interface initially located at the same place and divided by the thickness h attributed to the damaging zone. The pressure at each in-plane position of the interface is found as the average of the pressure of the upper and lower nodes of the interface. The in-plane pressure gradients are then obtained, based on the derivatives of the in-plane interpolation functions.

[9] Finally, the evolution of the permeability of potential cracks as a function of damage is postulated. In *Selvadurai* [2004], a quadratic relation between the damage-controlling parameter and the permeability was assumed within the framework of a stationary damage analysis. Here, a quadratic dependency on the damage variable itself will be considered as

$$k = k_0\left(1 + \beta D^2\right) \tag{9}$$

where k_0 is the initial permeability of the potential crack, and β is a factor that allows the fitting of the rate at which damage increases to the local permeability. The exponential damage evolution law (5) implies a lower damage development rate at the end of the softening slope, which will cause a saturation in the permeability increase at high damage values as is often observed in experiments, see Section 5. Note that this choice for the coupling between the mechanical and fluid

transport processes is essentially related to the assumption that the dominant macroscopic permeability alteration is mainly dictated by the evolution of cracking. This means that the pore changes within the grains themselves are assumed to be of a lower order. The choice of the quadratic relation (9) is mainly motivated by earlier experimental evidence available in [*Zoback and Byerlee*, 1975; *Shiping et al.*, 1994]. A linear dependency in (9) could also be used, delivering a proper fit, although slightly less accurate, with macroscopic experimental observations.

3. Computational Homogenization

3.1. Multiscale Modeling for Coupled Problems

[10] The use of multiscale computational and homogenization techniques has received increasing attention over the past decade. These methodologies first emerged in the field of mechanics of materials [*Smit et al.*, 1998], and were used to extract average properties of heterogeneous materials based on the properties of their constituents. They avoid the formulation of macroscopic constitutive laws by using scale transitions applied to RVEs, based on averaging theorems and laws postulated for constituents of the microstructure. Essentially, they transfer experimental parameter identification to lower scales on which phenomenologically simpler laws can be used, and require knowledge of the microstructural features. Such methodologies were used with various objectives, including the identification of average (macroscopic) material properties based on microstructural descriptions and postulated fine-scale laws, and the investigation of the microstructural origin of experimentally observed macroscopic effects.

[11] To date, geomechanical applications of multiscale techniques have mostly focused on the extraction of average properties of non-evolving microstructures for uncoupled mechanical properties of geomaterials [*Bouchelaghem et al.*, 2007], as well as for the mechanical behavior of porous materials with a weak coupling [*Benhamida et al.*, 2005]. Average permeability properties were derived using asymptotic homogenization procedure for uncoupled properties [*Santos and Sheen*, 2008]. Multiscale approaches coupling several scales originated because of difficulties in developing usable forms of constitutive models in simulations. Computationally, coarse discretizations can be supplemented with enriched basis functions deduced largely from microstructural features for uncoupled transport problems [*Zhang and Fu*, 2010]. Computational homogenization was reformulated to allow nested scale computational schemes in which finite element discretizations are used at both the macroscopic and fine scales simultaneously. This is achieved by scale transitions based on averaging theorems; applying macroscopic quantities on the RVEs in an average sense to construct a fine-scale boundary value problem. The responses obtained enable the replacement of a priori postulated macroscopic laws, when they are too complex to formulate, with closed-form constitutive relations at the fine scale only. This methodology was initially applied to mechanical problems, and was recently adapted for diffusive phenomena such as multiscale thermal conductivity [*Ozdemir et al.*, 2008a], assuming a stationary response at the fine scale, and by *Larsson et al.* [2010] for transient behavior at all scales.

3.2. Computational Homogenization for Mechanical Behavior

[12] In the mechanical description of a heterogeneous microstructure, a homogeneous equivalent material may be identified by means of computational homogenization techniques [*Anthoine*, 1995; *Kouznetsova et al.*, 2001]. Such techniques essentially apply a loading stimulus to an RVE containing the main microstructural features of the material. An equilibrium problem is then solved on the scale of the RVE, thereby allowing the identification of the properties of an equivalent averaged material. Based on a macroscopic strain **E** applied to an RVE of a given heterogeneous material, a displacement field within the microstructure is postulated as

$$\vec{u}(\vec{x}) = \mathbf{E}.\vec{x} + \vec{u}_f(\vec{x}) \tag{10}$$

where $\vec{x}$ is the position vector of a point within the RVE and $\vec{u}_f$ is a fluctuation field caused by the heterogeneity of the material. Computational homogenization classically rests on scale transition consistency arguments, among which is the requirement that the macroscopic strain is obtained as the volume average of the mesoscopic strain field ε derived from (10). Assuming a Cauchy continuum description, and with the help of the Green-Gauss theorem, this translates into

$$\frac{1}{V}\int_V \boldsymbol{\varepsilon}\, dV = \mathbf{E} + \oint_S \left(\vec{u}_f \vec{n}\right)^{sym} dS \tag{11}$$

Various choices can be made to ensure that the last integral of (11) vanishes. The most common choice consists of forcing the fluctuation $\vec{u}_f$ to be periodic at the boundary of the RVE. Using this periodicity assumption and the Hill-Mandel energy equivalence between the fine-scale and macroscopic descriptions, the macroscopic stress tensor is naturally obtained as the volume average of the microstructural stress tensor

$$\boldsymbol{\Sigma} = \frac{1}{V}\int_V \boldsymbol{\sigma} dV \tag{12}$$

These averaging operations do not depend on the material behavior postulated at the fine scale: any type of material behavior can be postulated at the fine scale. In the context of the finite element method, the periodicity of the microfluctuation field can be enforced by homogeneous linear connections between corresponding nodes of the boundary, if one ensures that identical meshes are used on the opposite faces of the RVE. In 3D, four controlling points, denoted 1 to 4 in Figure 2a, can be used to control the rigid body displacements and the macroscopic quantities (stress and deformation tensor) on the RVE. With these boundary conditions, the RVE equilibrium problem under macroscopic stress control can be solved by imposing forces $\vec{f}^{(a)}$ at the controlling points, which represent the action of the neighboring continuum on the RVE. The displacements of the controlling points energetically conjugated to the imposed controlling forces can be used to extract the macroscopic strain. The macroscopic stress is obtained as [*Kouznetsova et al.*, 2001]

$$\Sigma = \frac{1}{V}\sum_{a=1}^{4} \vec{f}^{(a)} \vec{x}^{(a)} dV \tag{13}$$

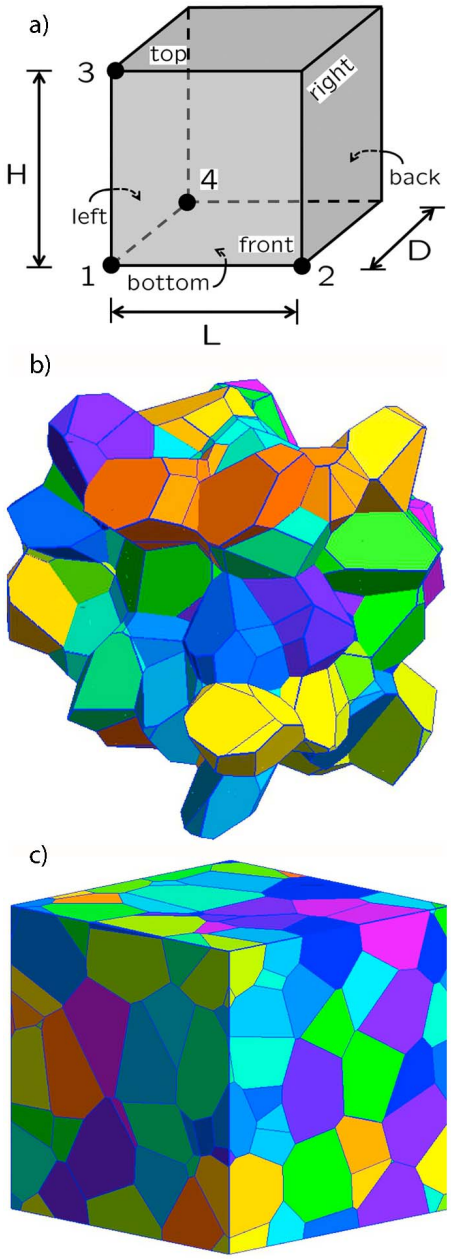

Figure 2. RVE definition: (a) control points of the 3D RVE, (b) Periodic Voronoi tesselation of 64 grains for a bounding box of 10 × 10 × 10 mm^3 - initial periodic set of grains, and (c) cubic arrangement of the set of grains obtained by trimming the initial set of grains.

The macroscopic stiffness of the material can be obtained as a by-product of solving the RVE boundary value problem. Upon convergence of the equilibrium iterations, the fine-scale discretized system of equations can be condensed at the controlling points. With such a condensed system [*Kouznetsova et al.*, 2001]

$$\left[K_M^*\right]\{\delta u_p\} = \left\{\delta f_p^*\right\} \tag{14}$$

where $[K_M^*]$ is the discretized fine-scale stiffness condensed at the controlling nodes and $\{\delta u_p\}$ and $\{\delta f_p^*\}$ represent the variations of displacements and tying forces at these nodes. The macroscopic tangent stiffness that relates variations of macroscopic stress to variations of macroscopic strain is obtained as

$${}^4\mathbf{L}_M = \frac{1}{V}\left(\sum_{a=1}^{4}\sum_{b=1}^{4}\vec{x}^{(a)}\mathbf{K}_M^{(ab)}\vec{x}^{(b)}\right)^{(rs)} \tag{15}$$

where the summations range over the control points and where (rs) indicates that only the right symmetric part of the tensor is taken. If damage laws are used at the fine scale, as is the case here, relations of the same type can be used to extract the (damaged) secant stiffness for a given state of the RVE.

3.3. Computational Homogenization for Steady State Flow Problems

[13] The objective is to identify the macroscopic averaged permeability tensor for a given local permeability distribution within the RVE. The homogenized permeability of the RVE can be evaluated using the upscaling scheme developed in *Ozdemir et al.* [2008a, 2008b] for heat conduction. A steady state balance equation is considered at the scale of the components within the RVE (non-transient), requiring the solution of the problem

$$\vec{\nabla}_m.\vec{q}_m = 0 \tag{16}$$

where $\vec{q}_m$ is the flux vector at the micro-scale. Assuming Darcy flow with a local permeability modified by the local damage state of the material, the following equation for the RVE level has to be solved

$$\vec{\nabla}_m.\left(-\frac{\mathbf{K}_m(\vec{x})}{\mu}.\vec{\nabla}p_m\right) = 0 \tag{17}$$

A periodic fluctuation $p_f(\vec{x})$ of the pressure field is assumed [*Ozdemir et al.*, 2008a] to describe the pressure profile in the RVE as

$$p_m(\vec{x}) = p_m^k + \vec{\nabla}_M p_M.\left(\vec{x} - \vec{x}^k\right) + p_f(\vec{x}) \tag{18}$$

where $\vec{\nabla}_M p_M$ is the macroscopic pressure gradient applied on the RVE, and p_m^k is the pressure of an arbitrary point in the RVE.

[14] Averaging constraints between the scales have to be defined in the same way as they were for the mechanical case. Since the pressure gradient is the driving force for flux, an averaging relation for the pressure gradient is required as

$$\vec{\nabla}_M p_M = \frac{1}{V}\int_V \vec{\nabla}_m p_m dV \tag{19}$$

[15] Using the relation (18) and the Green-Gauss theorem, the average of the fine-scale pressure gradient can be expressed as

$$\frac{1}{V}\int_V \vec{\nabla}_m p_m dV = \vec{\nabla}_M p_M + \frac{1}{V}\oint_S p_f \vec{n} dS \tag{20}$$

where the last integral of (20) vanishes and relation (19) is satisfied. The periodicity constraint on the pressure fluctuation field can be enforced by relations of the type

$$p_m^S - p_m^M = \vec{\nabla}_M p_M . \left(\vec{x}^S - \vec{x}^M\right) \tag{21}$$

between any pair of nodes related by a periodicity condition on a master (M) and a slave (S) surface. In contrast to the mechanical case, the relations (21) now require that non-homogeneous dependencies be defined between opposite RVE faces. Following *Ozdemir et al.* [2008a] the ensuing additional averaging relation is used to impose the consistency between scales of the product of the pressure gradient by the flux

$$\vec{\nabla}_M p_M . \vec{q}_M = \frac{1}{V} \int_V \vec{\nabla}_m p_m . \vec{q}_m \, dV \tag{22}$$

Combining the pressure gradient averaging (20) with the relationship (22), it can be shown that the macroscopic flux is automatically obtained as the RVE average of the fine-scale fluxes [*Ozdemir et al.*, 2008a]. Integrating (22) by parts and using fine-scale equilibrium (16), the averaging relation (22) can be expressed in boundary terms on the RVE

$$\vec{\nabla}_M p_M . \vec{q}_M = \frac{1}{V} \oint_S p_m q_{m_n} \, dS \tag{23}$$

where q_{m_n} is the normal flux at the boundary. Splitting this boundary integral in terms related to each face of the RVE, using the pressure periodicity constraints and local normal flux relations, and using the identity $\vec{\nabla}_m . (\vec{x}_m \vec{q}_m) = \vec{\nabla}_m . \vec{x}_m . \vec{q}_m + \vec{x}_m \left(\vec{\nabla}_m . \vec{q}_m\right) = \vec{q}_m$, the macroscopic flux is indeed identified as the RVE average of the fine-scale fluxes:

$$\vec{q}_M = \frac{1}{V} \int_V \vec{q}_m \, dV \tag{24}$$

The detailed steps of the derivation of relationship (24) starting from relationship (23) are given in Appendix B. The non-homogeneous linear constraints (21) can be directly implemented by means of a 'ghost' node procedure; thereby allowing the application of the macroscopic pressure gradients on the RVE. The homogenized permeability tensor of the RVE can be identified based on the link between the applied macroscopic pressure gradient terms at the 'ghost' nodes and the fluxes developing as a reaction to them. At equilibrium, the discretized system of equations for the transport problem can be condensed toward the 'ghost' nodes. Assuming that the origin of the axis system is located at one of the control nodes (i.e. $x_j^M = 0$ and $x_j^S = x_j$ in the periodicity connections), and using superscripts to denote 'ghost' (control) nodes and subscripts for dimensions in Einstein's summation convention, this condensation expresses fluxes at the controlling node (a) in terms of the applied macroscopic terms at the controlling node (b) as

$$q_{m_n}^{(a)} = \sum_{b=1}^{b=4} k^{(ab)} \left(\nabla_j p \; x_j\right)^{(b)} \tag{25}$$

where the summation spans the control nodes. Starting from the expression of the macroscopic flux

$$q_{M_i} = \frac{1}{V} \oint_S q_{m_n} x_i dS, \tag{26}$$

and using periodicity, the averaged flux is obtained from the 'reaction' fluxes at the controlling nodes similarly to the mechanical case as

$$q_{M_i} = \frac{1}{V} \sum_{a=1}^{a=4} q_{m_n}^{(a)} x_i^{(a)} \tag{27}$$

Substituting the condensed relation (25) into (27) allows the identification of the macroscopic (averaged) permeability $\mathbf{K}_{M_{ij}}$ as

$$\mathbf{K}_{M_{ij}} = \frac{\mu}{V} \sum_{a=1}^{a=4} \sum_{b=1}^{b=4} x_i^{(a)} k^{(ab)} x_j^{(b)} \tag{28}$$

It is emphasized that the fact that the macroscopic flux is expressed in terms of a boundary integral and subsequently in terms of controlling nodes quantities is merely a consequence of the periodicity assumption used in the developments. However, the macroscopic flux is obtained as a *volume* average of the fine-scale flux. As a result, all the local damaged permeabilities of the RVE are taken into account in the volume averaging procedure underlying relationship (28). This can be further realized by the fact that the condensed stiffness $k^{(ab)}$ actually takes them into account, being the condensation of the entire RVE microstructural stiffness which involves the permeability coefficients associated with all the RVE positions. This transport homogenization framework is equivalent to the asymptotic expansion techniques used in *Bear and Cheng* [2010]. Its flexibility, however, allows for subsequent incorporation into multilevel nested finite element solution schemes (known as FE^2) as illustrated in *Ozdemir et al.* [2008b], and it requires the fine-scale system to be solved (only once) for the entire permeability tensor to be extracted. As in the mechanical case, any modeling choice (constitutive laws, discretization technique) can be adopted for the fine-scale modeling. Note also that by its structure, the relation (28) yields a symmetric positive-definite averaged permeability tensor since the fine-scale condensed discretized stiffness $k^{(ab)}$ is itself symmetric and positive-definite.

4. Representative Volume Element Generation

[16] A complete state of the art for the generation of particulate media Representative Volume Elements (RVEs) can be found in *He* [2010]. Depending on the modeling strategy chosen for crack development (interface elements with cohesive laws), a specific RVE generation tool is required. Several RVE generation methodologies for random materials are available in the literature, mainly for inclusion-based systems. They are usually specific to the type of material under investigation, i.e. Random Sequential Addition in a RVE container (RSA) [*Cooper*, 1998; *Sherwood*, 1997], Discrete Element Method (DEM) [*Jia and Williams*, 2001; *Williams and Philipse*, 2003; *Stafford and Jackson*, 2010]

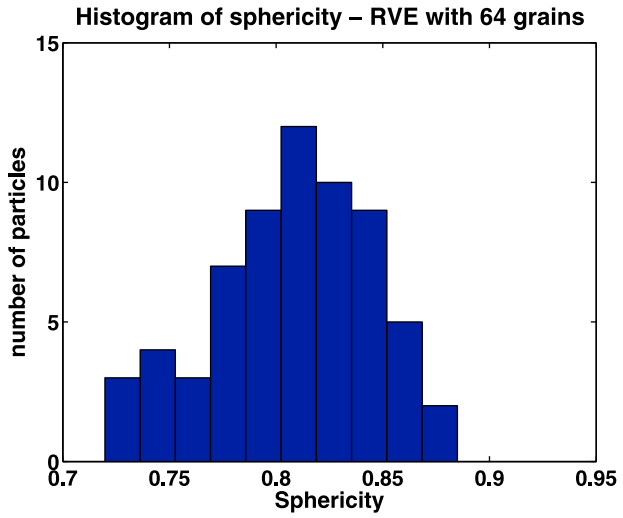

Figure 3. Sphericity distributions of the particles generated by the Voronoi 3D tesselation procedure within a $10 \times 10 \times 10$ mm^3 bounding box.

for particulate media and Voronoi tessellation methods for polycrystalline microstructures [*Rycroft et al.*, 2006; *Rycroft*, 2009; *Fritzen et al.*, 2009].

[17] For the representation of local failure within the RVEs based on interface elements, as presented in Section 2.1, a three-dimensional Voronoi tessellation is the most convenient RVE generation strategy, as it allows for the generation of random assemblies of grains that completely fill a prescribed space, based on an initial population of points. The generated grain boundaries consist of straight planar facets with random orientations and areas, depending on the original seed population [*Fritzen et al.*, 2009].

[18] In this paper, we use 3D RVEs based on the VORO++ library, see *Rycroft* [2009]. An illustration of a 64 grain assembly within a periodic unit cell of $10 \times 10 \times 10$ mm^3 is given in Figure 2b. In order to use the homogenization framework presented in Section 3, a parallelipipedic assembly is required. The periodic assembly obtained from VORO++ can be trimmed and re-organized according to the dimensions of the required RVE. This process results in a periodic cubic assembly of grains as illustrated in Figure 2c, and is equivalent to the original distribution. The RVE is next meshed in order to solve the mechanical and transport problems. The meshes were obtained using the GMSH mesher [*Geuzaine and Remacle*, 2009]. A surface periodic mesh at the boundary of the RVE is obtained using an extrusion functionality, before generating a complete 3D mesh.

[19] The grains are assumed to be linear elastic, without provisions for transgranular cracking. To assess the degree of validity of this assumption, by verifying that the probability of grain failure is indeed low as compared to intergranular failure, the sphericity of the grains within the aggregate can be used. The sphericity of a grain can be defined as the ratio of the surface area of a sphere (with the same volume as the grain) to the surface area of the grain

$$S_g = \frac{\pi^{\frac{1}{3}}(6V_g)^{\frac{2}{3}}}{A_g} \tag{29}$$

where V_g and A_g are the volume and surface area of the grain, respectively, with a spherical grain giving $S_g = 1$ and these are expected to require a higher energy to induce failure than elongated particles that can fail by flexure. The distribution of sphericity for the 64 grain assembly is shown in Figure 3. As can be seen, the sphericity distribution is centered on a value slightly above 0.8, indicating a low likelihood of transgranular fracture.

5. Damage-Induced Permeability Evolution

5.1. Problem Statement

[20] The ability for computational homogenization to represent damage-induced permeability evolution will now be considered. In order to provide a meaningful set of results, the principles presented in Section 3 will be applied to a RVE generated using the procedure described in Section 4 and material properties corresponding to a granite. Most of the fine-scale material properties are available in the literature. The 64 grain RVE generated in Section 4 is used. The grains are discretized with tetrahedral elements with quadratic interpolation of the displacement field (respective pressure field) in the mechanical (respective fluid transport) part of the analysis. Nodes are doubled and quadratic triangular cohesive interface elements are automatically incorporated at the planar boundaries between the grains. In order to use a physically realistic set of parameters, experimental results available for granitic materials are considered. The original set of experimental results for the mechanical properties and permeability evolution used are from *Souley et al.* [2001]. The elastic properties of the grains and of the cohesive interfaces are equal to the macroscopic ones and are taken from *Jiang et al.* [2010]. Typical fracture properties of granite can be obtained from the literature. Macroscopic values of the cohesion and of the friction angle in Lac du Bonnet granite were measured and discussed in *Martin and Chandler* [1994]. They showed that friction and cohesion are not activated simultaneously during the fracture process. As a result, the maximum cohesion that can be relied on for engineering purposes is less than half the unconfined compressive strength. From these tests, the average cohesion ranged from 30 MPa to 40 MPa, with the friction angle φ varying between 40° and 50°. Similar values were found for Barre granite [*Mahabadi et al.*, 2010] with a cohesion of 50 MPa, and a friction angle of 35°. The results obtained in *Martin and Chandler* [1994] were analyzed assuming a strain energy release rate at failure of 10^{-3} N/mm. Compressive properties reported in *Vasconcelos et al.* [2009] range from 26 to 160 MPa for the (unconfined) compressive strength with compressive fracture energies ranging from 2.3 N/mm to 10 N/mm for the pre-peak component and from 11 N/mm to 45 N/mm for the post-peak response. In *Vasconcelos et al.* [2008], the tensile strength of granite ranged from 2 MPa to 8 MPa, with a Mode-I fracture energy ranging between 0.1 N/mm and 0.3 N/mm, while tensile strengths in the range 6 MPa–10 MPa were reported for Barre granite [*Goldsmith et al.*, 1975] and for Lac du Bonnet granite [*Duevel and Haimson*, 1997]. Based on these sources, the values of the mechanical parameters for modeling potential cracks in subsequent computations were selected from the mentioned ranges and are reported in Table 1.

Table 1. Mechanical Parameters for Potential Cracks

	E (GPa)	ν	f_t (MPa)	c (MPa)	φ (°)	$G_{f,I}$ (N/mm)	h (mm)
Cracks	70	0.25	6	36	40	0.01	0.1

[21] With these values of the mechanical parameters, and for the 64 grain RVE generated in Section 4, the initial (undamaged) secant stiffness obtained through the homogenization procedure is nearly isotropic. The variation in the directional Young's moduli is less than 0.2%, showing that a sufficient number of grains is present within the RVE to avoid any bias related to the RVE size or interface orientation in the elastic range. Note that the mechanical properties of Table 1 will be assigned to all the cohesive interfaces present in the model. The heterogeneity in computations will therefore appear from the distributed orientations of the cohesive zone elements, and from their progressive degradation causing in turn stress redistributions in the microstructure. Since the RVE is obtained as a space tessellation, all grains are initially assumed to be in contact with their neighbors.

5.2. Damage Evolution in a Quasi-Brittle Material

[22] The 64 grain aggregate illustrated in Figure 2c is now subjected to triaxial tests at two confining stress levels. The mechanical responses of the RVE for two values of the confining pressure (10 MPa and 40 MPa) are given in Figures 4 and 5. The initial stages of the curves match reasonably well the experimental results obtained for Lac du Bonnet granite [*Jiang et al.*, 2010]. The transverse strains are correctly reproduced only for low stress levels; this deviation is related to the damage formulation used at the fine scale, which does not incorporate dilatancy effects. For both confining pressures, the stress-strain response of the RVE is accompanied by two graphical interpretations of the damage state. The cohesive interfaces for which the damage state is higher than 0.2 are depicted at various stages of the loading process (the deviatoric load is applied in the axial direction). In addition, the damage state is represented in a stereographic plot, illustrating the directional dependency of damage. A colored dot is given for each cohesive surface or a given orientation. The axial direction is perpendicular to the plane of the plot, i.e. a cohesive interface with a normal vector

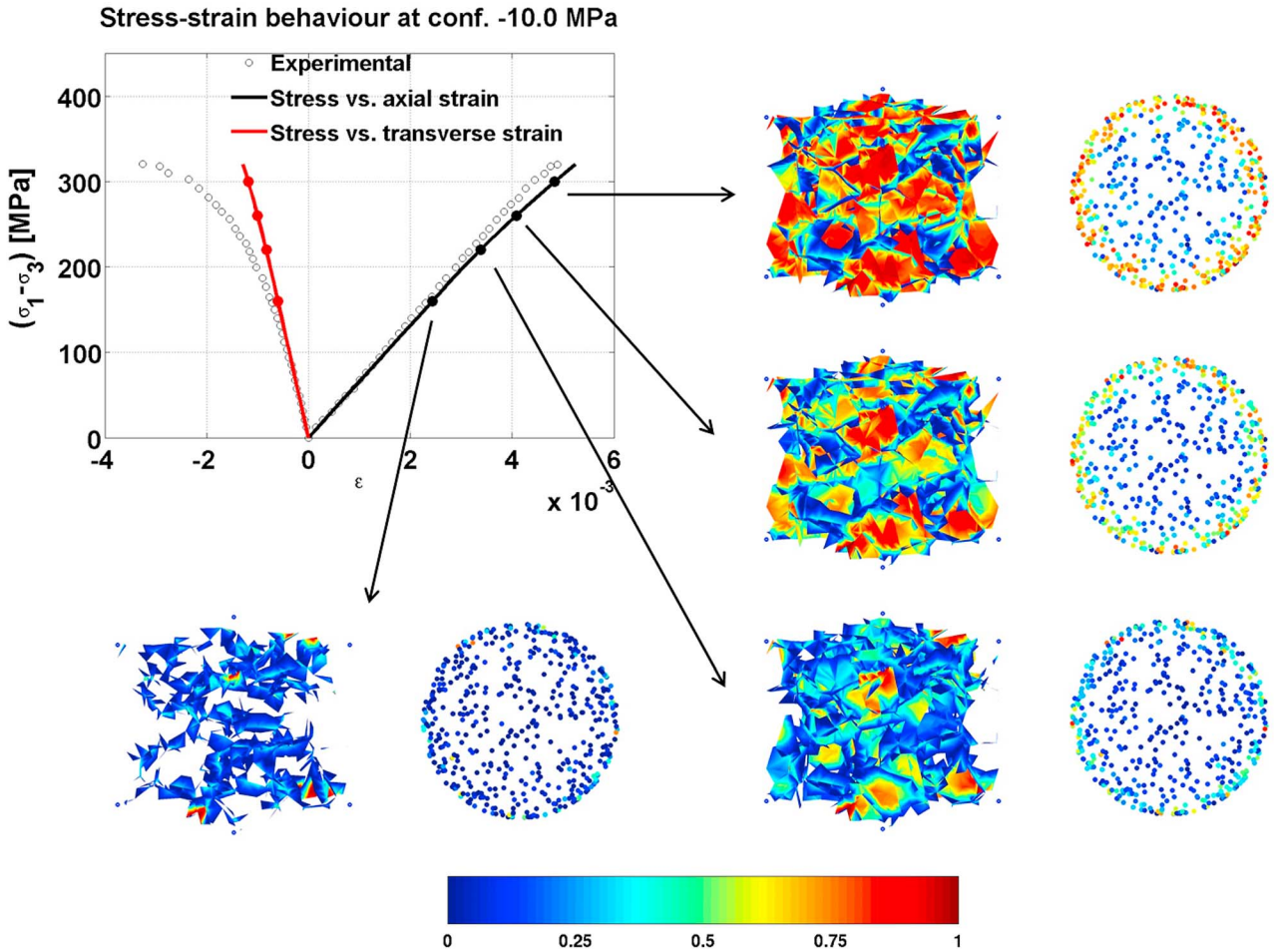

Figure 4. Stress-strain response and damage states of the RVE at confining pressure of 10 MPa. Only cohesive zones with a damage level of at least $D = 0.2$ are depicted. For each damage state depicted by a point on the stress-strain curve, the damage state is illustrated on a 3D view of the RVE. A stereographic view representing damage as a function of the orientation of the potential crack is also given (the longitudinal direction is perpendicular to the stereographic plot).

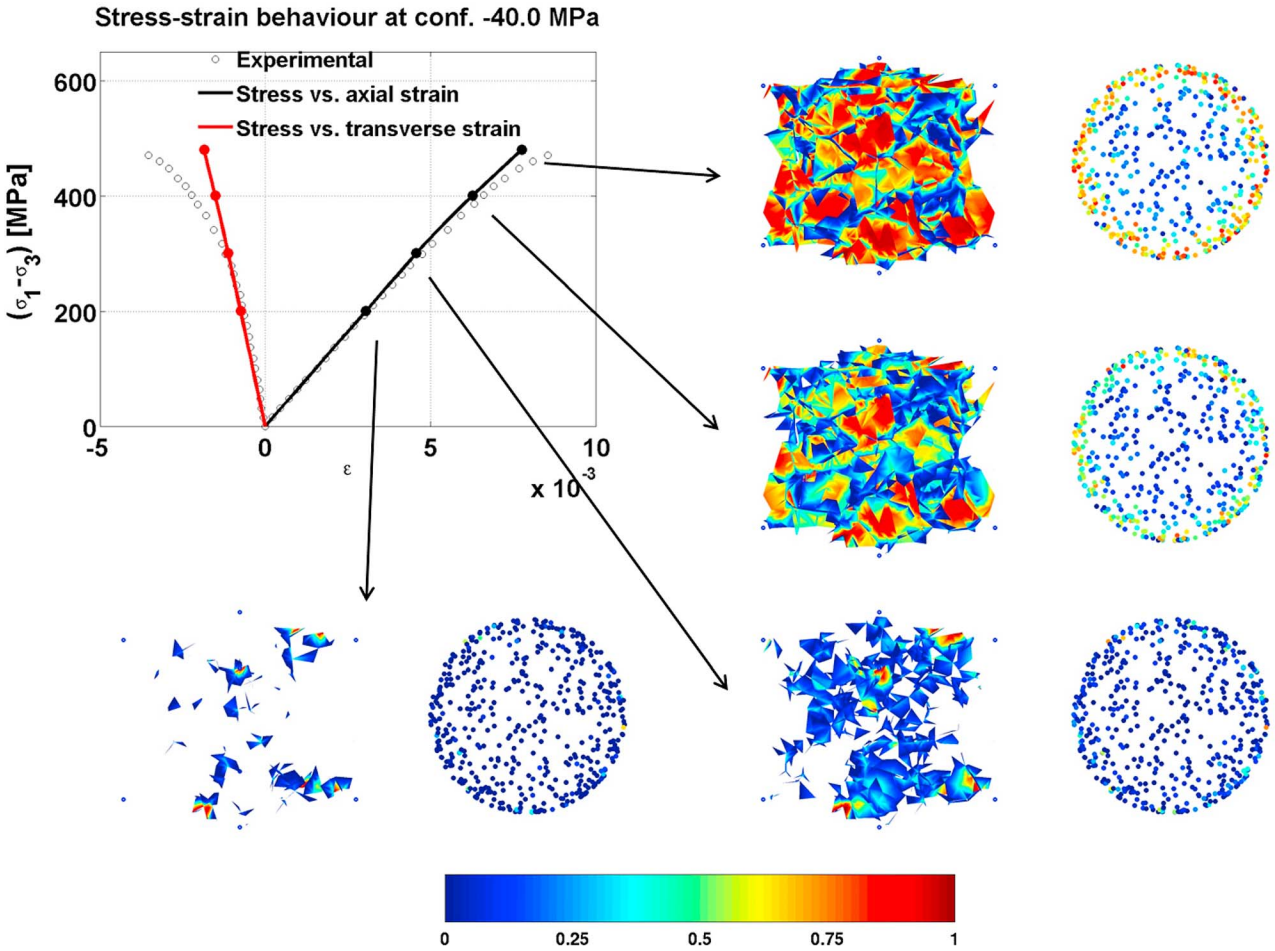

Figure 5. Stress-strain response and damage states of the RVE at confining pressure of 40 MPa. Only cohesive zones with a damage level of at least $D = 0.2$ are depicted. For each damage state depicted by a point on the stress-strain curve, the damage state is illustrated on a 3D view of the RVE. A stereographic view representing damage as a function of the orientation of the potential crack is also given (the longitudinal direction is perpendicular to the stereographic plot).

aligned with the axial direction is at the center of the plot. The distribution of points in the stereographic plot also illustrates the cracking orientation representativity of the RVE used: all cracking orientations are present, thereby allowing a general average cracking scheme to develop. Note that the proposed computations are well below the peak of the stress-strain response, which is confirmed by the experimental peak values reported for Lac du Bonnet granite [*Wang and Tonon*, 2009], where the peak values were 215 MPa, 350 MPa and 440 MPa respectively, for confining pressures of (0, 10 and 20) MPa.

[23] As can be seen in Figure 4, for a confining pressure of 10 MPa, an extended damage state is reached at a deviator stress of 200 MPa. The directional plots show that vertically oriented interfaces (i.e. parallel to the longitudinal loading direction) are damaged the most (outer circumferential points in stereographic plots). This agrees with the experimental observations reported in *Oda et al.* [2002] for granite. Even though the peak value of the stress-strain response has not been reached, a continuous damage path can be found, allowing an increase in the average permeability of the sample (see below). For a higher confining stress level of 40 MPa, similar results are seen in terms of damage progression and preferential orientation (Figure 5). As expected [*Yuan and Harrison*, 2005], the damage growth is delayed as a result of the confining normal stress in the damage criterion applied for the cohesive interfaces (Mohr-Coulomb-like criterion). The damage state found at $(\sigma_1 - \sigma_3) = 300$ MPa is much less extensive for the higher confining pressure (Figure 5) than for the lower one (Figure 4).

[24] The directional dependency of damage can be assessed quantitatively using the generalization of the relation (15) to the homogenized secant stiffness. Based on the initial and damaged homogenized secant stiffness tensors, the degradation of the normal stiffness components in the axial and transverse directions can be deduced. These degradation ratios are depicted in Figure 6 for both confining pressures. The normal stiffness degradation appears almost doubled in the transverse directions with respect to the principal loading direction for both confining pressure levels. This is consistent with the observations from the stereographic plots, and will be analyzed in relation to the directional permeability evolution.

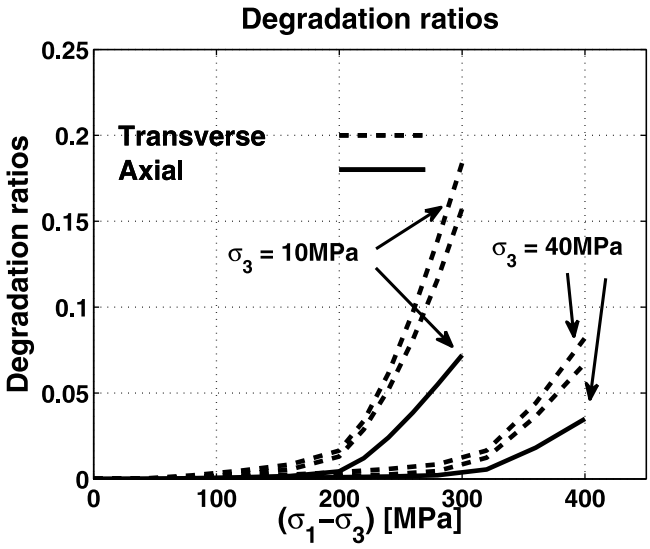

Figure 6. Degradation of normal stress components.

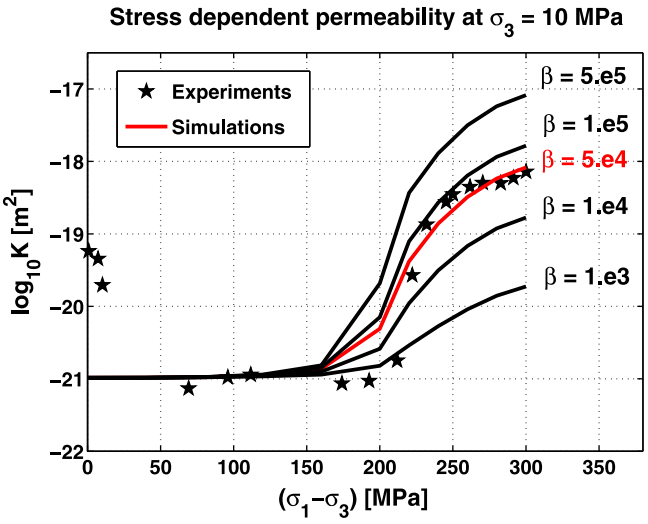

Figure 7. Axial permeability evolution as a function of the stress level for a confining pressure of 10 MPa for various values of the damage coupling parameter β.

5.3. Damage-Induced Permeability Evolutions

[25] Apart from the references cited previously, data on permeability evolution with the stress state is relatively scarce in the literature. For Lac du Bonnet granite, permeability evolution data was obtained for a confining pressure of 10 MPa in *Souley et al.* [2001]. This data was used in *Jiang et al.* [2010] for illustration of a closed-form damage-permeability model.

[26] Since no initial crack closure is incorporated in the modeling and since crack closure effects are expected to strongly depend on the level of confinement, a first attempt was conducted to fit data for a single confining pressure (of 10 MPa). An initial permeability of $k_0 = 10^{-21}$ m^2, corresponding to the lowest value obtained experimentally [*Souley et al.*, 2001], is used for both the grains and the cohesive zones. The initial permeability tensor obtained computationally for the 64 grain RVE is almost isotropic.

[27] Using the various damage states presented in Figure 4, the coupling parameter β can be adjusted to fit the increase in axial permeability caused by the damage development under a confining pressure of 10 MPa. In Figure 7, an optimal fit is found in the permeability vs. loading response for a value of $\beta = 5.10^4$. A permeability increase from its lowest value by almost three orders of magnitude is obtained with this value of the parameter, consistent with most experimental observations for quasi-brittle rocks.

[28] The evolution of permeability as a function of the applied loading strongly depends on the level of confinement with a inhibited overall damage evolution for increasing confinement. As noted in *Yuan and Harrison* [2005], this results in an inhibited permeability evolution as a function of the loading level for increasing confining pressures, as illustrated experimentally in *Jiang et al.* [2010] for basalt. This effect is properly reproduced by the RVE computations as illustrated in Figure 8, keeping the same value of the coupling parameter β.

[29] Focusing on the damage-induced permeability evolution, the effect of the confining pressure can be analyzed using data reported in *Souley et al.* [2001] for a confining pressure of 5 MPa for Senones granite, which has approximately the same mechanical properties as the Lac du Bonnet granite, *Shao et al.* [1999]. Keeping the value of the coupling parameter $\beta = 5.10^4$ (Figure 7), a simulation is performed for a confining pressure of 5 MPa. As can be noted from the experimental results given in Figure 9 [*Souley et al.*, 2001], the permeability at the start of the deviatoric phase of loading is quite different for both confining pressures and accompanied by a decrease in the permeability at the start of the deviatoric loading for a confining pressure of 10 MPa. This may be due, at least in part, to crack closure effects. No initial crack closure effect is incorporated in the fine-scale modeling within the RVE. To compensate for this fact while focusing on damage-induced permeability change, a different initial undamaged permeability of $k_0 = 2.10^{-19}$ m^2 is used

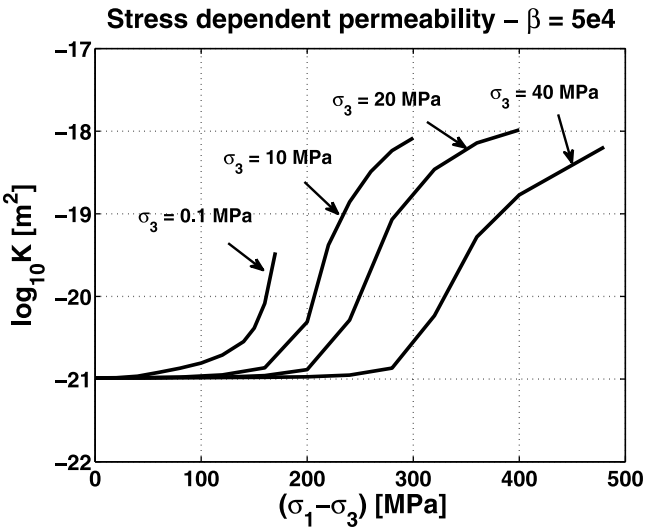

Figure 8. Confining pressure dependency of permeability evolution for the coupling parameter identified in Figure 7.

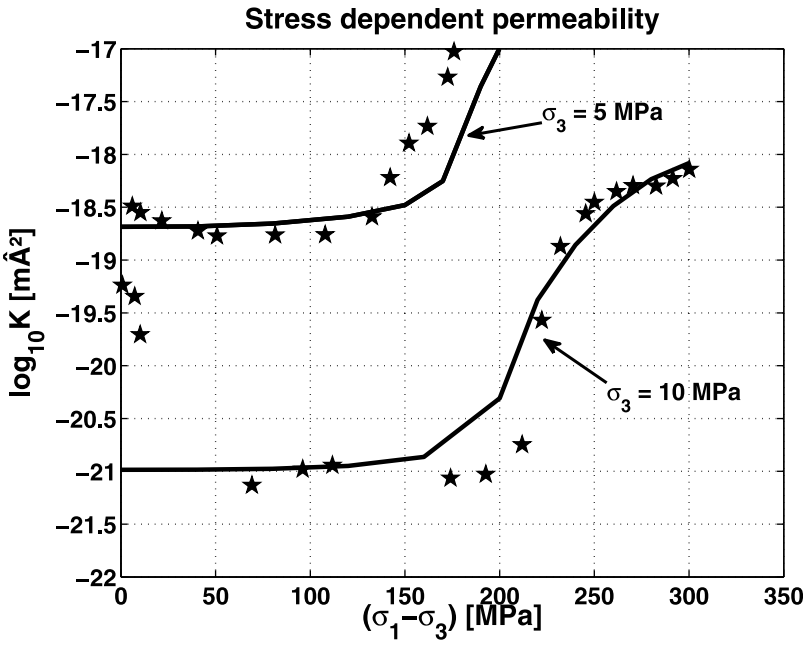

Figure 9. Axial permeability evolution as a function of the stress level for a confining pressure of 5 MPa and 10 MPa. Star markers denote experimental results reproduced after [*Souley et al.*, 2001]. Experimental results at a confining pressure of 5 MPa relate to Senones granite, while results at a confining pressure of 10 MPa relate to Lac du Bonnet granite.

in the simulations for the 5 MPa confining pressure, while the value $k_0 = 10^{-21}$ m^2 is kept for the 10 MPa confining pressure. Based on these values, the damage coupling parameter fitted on the 10 MPa confining pressure allows a reasonable fit of the experimental results at a confining pressure of 5 MPa as well, which is illustrated in Figure 9.

6. Discussion

[30] The results reported in the paper show that computational homogenization allows a qualitative assessment of permeability evolution caused by mechanical damage, usually interpreted in terms of stiffness degradation. The coupling between mechanical degradation and transport in the joints of a polycrystalline material can indeed reproduce an increase in permeability by several orders of magnitude as a result of local damage within the microstructure of the material, before the peak of the stress-strain response.

[31] A number of assumptions that are sometimes introduced in closed-form models for the sake of simplicity are avoided in computational homogenization techniques, although at the expense of a greater computational effort. Among such additional effects, the cohesive zones are free to open/close depending on the local stress state with no a priori assumption introduced concerning the connectivity of cracks, i.e. continuous channels naturally appear in the formulation. This generality is important in the context of fluid transport since permeability increases are related to continuous crack paths developing in the material. No additional assumption is made on the relationship between the macroscopic and fine-scale pressure gradients, i.e. the local pressure gradients are not taken equal to the macroscopic ones, but are rather imposed by the local microstructural events. The approach rests on postulated laws at the fine scale, with the potential added benefit of ease of assessment of other more physically motivated fine-scale constitutive laws. This offers the possibility of introducing modeling assumptions in a progressive manner, in order to single out fine-scale features that can have a dominant influence on macroscopic scale observations. It also allows effects of complex phenomena to be quantified, such as damage-induced anisotropy, without making predefined assumptions that are sometimes difficult to verify.

[32] A typical question related to damage and permeability evolution is the validity of a scalar damage description of the degradation process, and hence of a scalar effective permeability evolution. The proposed framework allows the degree of validity of such an assumption to be assessed. The directional permeability evolution along the axial and transverse directions, corresponding to the diagonal components of the permeability tensor are plotted in Figure 10 for various confining pressures. Even though a scalar damage description is adopted at the local scale, the averaged mechanical response of the material exhibits anisotropy as illustrated in Figure 6. As can be noted from Figure 10, the validity of a scalar description of the effective permeability evolution depends on the applied deviatoric stress. Globally, and for the considered set of parameters, the increase of permeability in all directions is several orders of magnitude for all three diagonal components of the permeability tensor. However, at intermediate stages of loading, differences can appear between the axial and transverse directions, with the axial permeability 2 to 3 times lower than the transverse components [*Simpson et al.*, 2001]. Depending on the application, a scalar permeability evolution can therefore be considered, by extracting the geometric mean of directional permeabilities, as illustrated in Figure 10 [*Selvadurai and Selvadurai*, 2010].

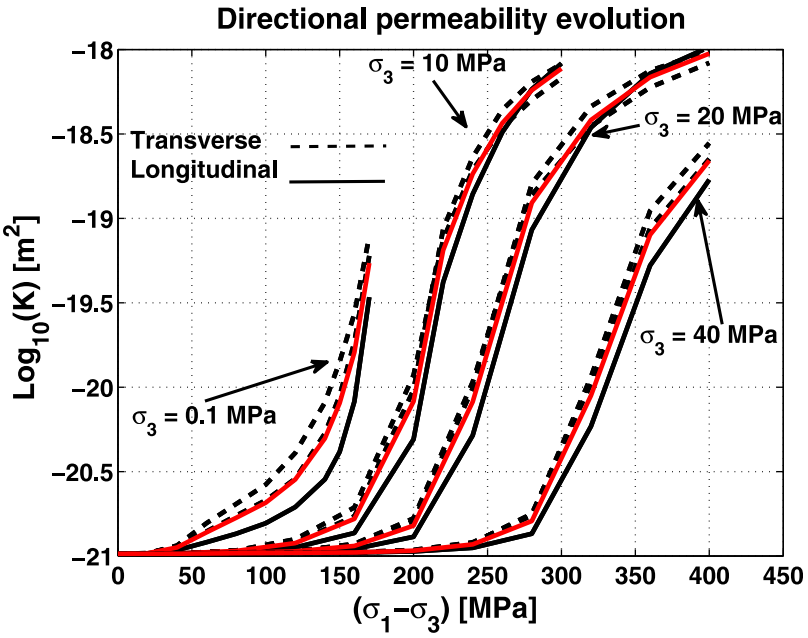

Figure 10. Directional permeability evolution as a function of the stress level for various confining pressures. Dashed lines represent the permeability along transverse directions, while continuous lines represent the permeability in the longitudinal (axial) direction. The red lines represent the geometric mean of all three diagonal components of the tensor.

[33] An inherent limitation of the proposed approach is that meaningful fine-scale behavior features are required, which are sometimes difficult to determine experimentally in terms of morphology (geometrical arrangements and shape of the phases) and mechanical properties. The results presented here are based on a purely phenomenological local coupling, introducing stiffness degradation effects in local transport properties by means of a coupling parameter β to be fitted based on experimental results. The β parameter remains a phenomenological parameter as no specific lower-scale argument is used in order to derive its value at this stage. A variation of this parameter can thus cover various lower-scale origins of the macroscopically observed permeability increase. Also note that a linear dependency instead of the quadratic relationship (9) would, with the same value of the local fully damaged permeability (i.e. same value of β) deliver macroscopic permeability evolutions very close to those reported here.

[34] The results shown in Figure 9, however, indicate that the same parameter value appears to correctly reproduce the permeability evolution for other confining conditions. It is emphasized that the phenomenological nature of the fine-scale coupling postulated here for cracking is not linked to an inherent limitation of the upscaling methodology. With the chosen periodicity assumption, the upscaling framework presented in Section 3 is completely independent of the laws postulated at the fine scale, as long as the RVE average response remains in the pre-localization regime, and as long as the mechanical and fluid transport problems can be solved independently. It can therefore be used with more physically motivated local mechanical laws, including dilatancy and contractancy. Future improvements to the model could be incorporated to address additional fine-scale phenomena, such as grain cracking and crushing; or pore collapse and initial crack closure that potentially leads to drastic permeability decrease as reported in [*Zhu et al.*, 2007; *Zhu and Wong*, 1997; *Jiang et al.*, 2010].

7. Concluding Remarks

[35] The permeability evolution of quasi-brittle geomaterials can be assessed using computational homogenization techniques applied on Representative Volume Elements (RVEs) of typical microstructures. Based on a micro-scale description of the internal structure of such materials and based on classical closed-form mechanical and transport laws postulated on their micro-scale, averaging theorems allow the extraction of meaningful information on the degree of variation of the permeability with the degree of damage. The general nature of the averaging framework allows the potential appearance of complex behaviors such as anisotropy at the macro-scale with simple isotropic laws postulated at the micro-scale.

[36] With a periodic RVE generation tool based on 3D Voronoi tesselation principles and with the help of fine-scale constitutive laws and of a local coupling between damage and permeability evolutions, the ability of the framework to extract damage-induced macroscopic permeability evolution is illustrated. Based on a set of mechanical and transport parameters matching a granite-type material, the load-induced evolution of averaged permeabilities by several orders of magnitude can be fitted. Starting from the fitting of the coupling parameter at a given confining pressure, computational results show that the framework is capable of reproducing the trend in the permeability evolution for other confining stress states. The development of anisotropy in both the mechanical and transport properties of the material is a natural by-product of the methodology. The computations

show that permeability anisotropy is a potential feature of such materials, even though directional permeability evolution globally remains at the same order of magnitude for the set of parameters considered.

[37] It is noted that the versatility of the framework allows additional extensions to incorporate more physically based fine-scale descriptions. In view of the experimental evidence available in the literature, the following aspects could be incorporated in the future to shed light on their relative importance. First, existing (initial) crack (or pore) closure could be incorporated in an average sense in the cohesive zone formulation used here. This would allow the variability of the permeabilities to be taken into account at the start of the deviatoric loading phase for different confinement conditions, as illustrated by the results reported in *Souley et al.* [2001]. Secondly, the permeability evolution during the deviatoric loading phase could be analyzed using physical laws incorporating contractancy and dilatancy of potential failure zones, in an approach similar to *Nguyen and Selvadurai* [1998] in terms of hydraulic aperture variations in joints.

Appendix A: Mechanical Cohesive Law Relationships

[38] The damage criterion illustrated in Figure 1 in the space of stress components of the cohesive zone is a composite criterion. It is translated in the space of relative displacement across the cohesive zone, since the damage formulation is strain-based. For the tension part of the criterion expressed in the stress space, damage is assumed to initiate if

$$\sigma > f_t \tag{A1}$$

where f_t is the tensile strength. This condition is translated as

$$\frac{\sigma}{k_n} > \frac{f_t}{k_n} \quad \text{or} \quad \delta_n > \kappa_i \tag{A2}$$

where κ_i is defined as the threshold for the normal relative displacement from which damage occurs. The shearing part of the criterion is expressed in the space of stress components as

$$\sigma \tan\varphi + \sqrt{\tau_s^2 + \tau_t^2} - c > 0 \tag{A3}$$

Expressing the stress components in terms of the relative displacements ($\sigma = k_n\delta_n$, $\tau = k_t\delta_t$), one obtains

$$\frac{f_t}{c}\delta_n \tan\varphi + \frac{k_t f_t}{k_n c}\sqrt{\delta_s^2 + \delta_t^2} > \underbrace{\frac{f_t}{k_n}}_{\kappa_i} \tag{A4}$$

The composite criterion is obtained by combining both expressions. The active part of the criterion is the one for which the quantity to compare to κ_i is the largest. Relationship (4) therefore expresses the scalar equivalent relative displacement measure to compare to κ_i for the complete criterion).

[39] The derivation of equation (6) follows immediately from relations (4) applied for mode I and pure mode II loading with the exponential damage evolution given in (5). Using the following notations to shorten the expressions

$$\kappa_i = \frac{f_t}{k_n} \quad ; \quad \theta = \frac{f_t}{G_{f,I}} \tag{A5}$$

the exponential damage evolution law is written as

$$D(\kappa) = 1 - \frac{\kappa_i}{\kappa} e^{-\theta(\kappa - \kappa_i)} \tag{A6}$$

The mode I fracture energy can be recovered as the area under the normal stress-normal relative displacement curve

$$G_{f,I} = \int_{\kappa_i}^{+\infty} \sigma d\delta_n(\kappa) \tag{A7}$$

Using the previous notations, and substituting the damage evolution law with a purely monotonic loading (i.e. $\delta_n = \kappa$) one finds

$$\int_{\kappa_i}^{+\infty} k_n \kappa_i e^{-\theta(\kappa - \kappa_i)} d\kappa = \frac{k_n \kappa_i}{\theta} = G_{f,I} \tag{A8}$$

Similarly, under pure mode II loading, the tangential stress-relative displacement relationship is given by

$$\tau = (1 - D(\kappa))k_t\delta_t = \left(\frac{\kappa_i}{\kappa} e^{-\theta(\kappa - \kappa_i)}\right) k_t\delta_t \tag{A9}$$

Based on the damage criterion (4), for a pure shear case, the shearing relative displacement is related to κ according to

$$\kappa = \delta_{eq} = \frac{f_t}{c}\frac{k_t}{k_n}\delta_t \tag{A10}$$

Isolating δ_t from this equation, substituting it in the expression of the tangential stress-relative displacement relation, and defining the mode II fracture energy as the area under that curve, one obtains

$$\begin{aligned} G_{f,II} &= \int_{\kappa_i}^{+\infty} \tau d\delta_t(\kappa) = \int_{\kappa_i}^{+\infty} \frac{\kappa_i}{\kappa} e^{-\theta(\kappa - \kappa_i)} k_t\delta_t(\kappa) d\delta_t(d\kappa) \\ &= \left(\frac{c}{f_t}\right)^2 \left(\frac{k_n}{k_t}\right) G_{f,I} \end{aligned} \tag{A11}$$

Appendix B: Averaging Relation for Fluid Transport Problem

[40] Relationship (24) establishing the consistency of the flux between scales can be demonstrated as follows. Starting from relationship (23)

$$\frac{1}{V}\int_V \vec{\nabla}_m p_m . \vec{q}_m \, dV = \frac{1}{V}\oint_S p_m q_{m_n} \, dS \tag{B1}$$

the right-hand side can be developed by splitting the integral along the faces of the RVE as (only one pair of opposite faces of the RVE is explicitly written for brevity)

$$\frac{1}{V}\oint_S p_m q_{m_n} \quad dS = \frac{1}{V}\int_{S^{\text{left}}} p_m^{\text{left}} q_{m_n}^{\text{left}} dS + \frac{1}{V}\int_{S^{\text{right}}} p_m^{\text{right}} q_{m_n}^{\text{right}} dS + \ldots \tag{B2}$$

Using the anti-periodicity of the normal flux at the boundary of the cubic RVE, these terms can be reformulated as

$$\frac{1}{V}\oint_S p_m q_{m_n}\, dS = \frac{1}{V}\int_{S^{\text{left}}} p_m^{\text{left}} q_{m_n}^{\text{left}} dS + \frac{1}{V}\int_{S^{\text{right}}} p_m^{\text{right}}\left(-q_{m_n}^{\text{left}}\right) dS + \ldots \tag{B3}$$

Assembling the terms of the opposite faces, the closed integral becomes

$$\frac{1}{V}\oint_S p_m q_{m_n}\, dS = \frac{1}{V}\int_{S^{\text{left}}} \left(p_m^{\text{left}} - p_m^{\text{right}}\right) q_{m_n}^{\text{left}} dS + \ldots \tag{B4}$$

Further, using relation (21), the pressure variation between points of opposite faces can be related to the macroscopic pressure gradient, and the boundary integral becomes

$$\frac{1}{V}\oint_S p_m q_{m_n}\, dS = \frac{1}{V}\vec{\nabla}_M p_M . \left[\int_{S^{\text{left}}} \left(\vec{x}^{\text{right}} - \vec{x}^{\text{left}}\right) \vec{q}_m \vec{n}^{\text{right}} dS + \ldots\right] \tag{B5}$$

The consistency between scales of the product of the pressure gradient by the flux becomes

$$\vec{\nabla}_M p_M . \vec{q}_M = \frac{1}{V}\oint_S p_m q_{m_n}\, dS = \frac{1}{V}\vec{\nabla}_M p_M . \oint_S \vec{x} q_{m_n} dS \tag{B6}$$

As a result, the macroscopic flux can be expressed in terms of a boundary integral involving the normal fluxes at the boundary

$$\vec{q}_M = \frac{1}{V}\oint_S \vec{x}_m q_{m_n} dS \tag{B7}$$

It is emphasized that the averaging operation is a true volume averaging, the simplification toward a surface integral being the result of the periodicity assumption (and of the steady state equilibrium at the fine scale). Further, the boundary integral can be reformulated to show that the macroscopic flux is the volume average of the fine-scale fluxes

$$\vec{q}_M = \frac{1}{V}\oint_S \vec{x}_m q_{m_n} dS = \frac{1}{V}\oint_S \vec{x}_m\, \vec{q}_m . \vec{n} dS = \frac{1}{V}\int_V \vec{\nabla}_m . (\vec{x}_m \vec{q}_m) dV \tag{B8}$$

Using the identity

$$\vec{\nabla}_m . (\vec{x}_m \vec{q}_m) = \vec{\nabla}_m . \vec{x}_m . \vec{q}_m + \vec{x}_m \left(\vec{\nabla}_m . \vec{q}_m\right) = \vec{q}_m \tag{B9}$$

in which the last term between parentheses vanishes due to steady state equilibrium at the fine scale, the macroscopic flux is finally obtained as

$$\vec{q}_M = \frac{1}{V}\int_V \vec{q}_m\, dV \tag{B10}$$

[41] **Acknowledgments.** The work described in this paper was achieved during the tenure of a Marie Curie Outgoing Fellowship awarded to the first author by the European Commission under project MULTIROCK. The support from F.R.S-FNRS Belgium for intensive computational facilities through grant 1.5.032.09.F is also acknowledged. The first author is grateful for the facilities provided by the Environmental Geomechanics group, Department of Civil Engineering and Applied Mechanics, McGill University.

References

Anthoine, A. (1995), Derivation of the in-plane elastic characteristics of masonry through homogenization theory, *Int. J. Solids Struct.*, *32*, 137–163.

Bear, J., and A. H. D. Cheng (2010), *Modeling Groundwater Flow and Contaminant Transport*, *Theory Appl. Transp. Porous Media*, vol. 23, Springer, Dordrecht, Netherlands.

Biot, M. A. (1941), General theory of three-dimensional consolidation, *J. Appl. Phys.*, *12*, 155–164.

Benhamida, A., I. Djeran-Maigre, H. Dumontet, and S. Smaoui (2005), Clay compaction modelling by homogenisation theory, *Int. J. Rock Mech. Min. Sci.*, *42*, 996–1005.

Bouchelaghem, F., A. Benhamida, and H. Dumontet (2007), Mechanical damage behaviour of an injected sand by periodic homogenization method, *Comp. Mater. Sci.*, *38*, 473–481.

Cooper, D. W. (1998), Random-sequential-packing simulations in three dimensions for spheres, *Phys. Rev. A*, *38*, 522–524.

Coussy, O. (1995), *Mechanics of Porous Continua*, John Wiley, New York.

Detournay, E., and A. H.-D. Cheng (1993), Fundamentals of poroelasticity, in *Comprehensive Rock Engineering: Principles, Practice and Projects*, vol. 2, *Analysis and Design Method*, edited by J. Hudson, pp. 113–171, Pergamon, Oxford, U. K.

Duevel, B., and B. Haimson (1997), Mechanical characterization of pink Lac du Bonnet granite: Evidence of nonlinearity and anisotropy, *Int. J. Rock Mech. Min. Sci.*, *34*, 117.e1–117.e18.

Fritzen, F., T. Bohlke, and E. Schnack (2009), Periodic three-dimensional mesh generation for crystalline aggregates based on Voronoi tessellations, *Comput. Mech.*, *43*, 701–713.

Geers, M. G. D. (1999), Enhanced solution control for physically and geometrically non-linear problems. Part I—The subplane control approach, *Int. J. Numer. Methods Eng.*, *46*, 177–204.

Geuzaine, C., and J.-F. Remacle (2009), Gmsh: A three-dimensional finite element mesh generator with built-in pre- and post-processing facilities, *Int. J. Numer. Methods Eng.*, *79*(11), 1309–1331.

Goldsmith, W., J. L. Sackman, and C. Ewert (1975), Static and dynamic fracture strength of Barre granite, *Int. J. Rock Mech. Sci. Geomech. Abstr.*, *13*, 303–309.

He, H. (2010), Computational modelling of particle packing in concrete, PhD thesis, Delft Univ. of Technol., Delft, Netherlands.

Hu, D. W., Q. Z. Zhu, H. Zhou, and J. F. Shao (2010), A discrete approach for anisotropic plasticity and damage in semi-brittle rocks, *Comp. Geotech.*, *37*, 658–666.

Jia, X., and R. A. Williams (2001), A packing algorithm for particles of arbitrary shapes, *Powder Technol.*, *120*, 175–186.

Jiang, T., J. F. Shao, W. Y. Xu, and C. B. Zhou (2010), Experimental investigation and micromechanical analysis of damage and permeability variation in brittle rocks, *Int. J. Rock. Mech. Min. Sci.*, *47*, 703–713.

Kiyama, T., H. Kita, Y. Ishijima, T. Yanagidani, K. Akoi, and T. Sato (1996), Permeability in anisotropic granite under hydrostatic compression and triaxial compression including post-failure region, in *Rock Mechanics: Tools and Techniques—Proceedings of the 2nd North American Rock Mechanics Symposium*, edited by M. Aubertin, F. Hassani, and H. Mitri, pp. 1643–1650, A. A. Balkema, Brookfield, Vt.

Kouznetsova, V. G., W. A. M. Brekelmans, and F. T. P. Baaijens (2001), An approach to micro-macro modeling of heterogeneous materials, *Comp. Mech.*, *27*(1), 37–48.

Larsson, F., K. Runesson, and F. Su (2010), Computational homogenization of uncoupled consolidation in micro-heterogeneous porous media, *Int. J. Num. Anal. Methods Geomech.*, *34*(14), 1431–1458.

Lotfi, H. R., and B. Shing (1994), Interface model applied to fracture of masonry structures, *J. Struct. Eng.*, *120*(1), 63–80.

Mahabadi, O. K., B. E. Cottrell, and G. Grasselli (2010), An example of realistic modelling of rock dynamics problems: FEM/DEM simulation of dynamic brazilian test on Barre granite, *Rock. Mech. Rock. Eng.*, *43*, 707–716.

Mahyari, A. T., and A. P. S. Selvadurai (1998), Enhanced consolidation in brittle geomaterials susceptible to damage, *Mech. Cohesive Frict. Mater.*, *3*, 291–303.

Martin, C. D., and N. A. Chandler (1994), The progressive fracture of Lac du Bonnet granite, *Int. J. Rock Mech. Min. Sci. Geomech. Abstr.*, *31*, 643–659.

Mercatoris, B. C. N., and T. J. Massart (2011), A coupled two-scale computational scheme for the failure of periodic quasi-brittle thin planar shells and its application to masonry, *Int. J. Numer. Methods Eng.*, *85*, 1177–1206.

Nguyen, T. S., and A. P. S. Selvadurai (1998), A model for coupled mechanical and hydraulic behaviour of a rock joint, *Int. J. Num. Anal. Methods Geomech.*, *22*, 29–48.

Oda, M., T. Takemura, and T. Aoki (2002), Damage growth and permeability change in triaxial compression tests of Inada granite, *Mech. Mater*, *34*, 313–331.

Ozdemir, I., W. A. M. Brekelmans, and M. G. D. Geers (2008a), Computational homogenization for heat conduction in heterogeneous solids, *Int. J. Numer. Methods Eng.*, *73*, 185–204.

Ozdemir, I., W. A. M. Brekelmans, and M. G. D. Geers (2008b), FE^2 computational homogenization for the thermo-mechanical analysis of heterogeneous solids, *Comp. Methods Appl. Mech. Eng.*, *198*, 602–613.

Paria, G. (1963), Flow of fluid through porous deformable solids, *Appl. Mech. Rev.*, *16*, 901–907.

Peerlings, R. H. J., R. de Borst, W. A. M. Brekelmans, and J. H. P. de Vree (1996), Gradient-enhanced damage for quasi-brittle materials, *Int. J. Numer. Methods Eng.*, *39*, 3391–3403.

Rice, J. R., and M. P. Cleary (1976), Some basic stress diffusion solutions for fluid-saturated elastic porous media with compressible constituents, *Rev. Geophys.*, *14*(2), 227–241.

Rycroft, C. H. (2009), Voro++: A three-dimensional Voronoi cell library in C++, *Chaos*, *19*, 041111, doi:10.1063/1.3215722.

Rycroft, C. H., G. S. Grest, J. W. Landry, and M. Z. Bazant (2006), Analysis of granular flow in a pebble-bed nuclear reactor, *Phys. Rev. E*, *74*, 021306, doi:10.1103/PhysRevE.74.021306.

Santos, J. E., and D. Sheen (2008), Derivation of Darcy's law for a porous medium composed of two solid phases saturated by a single phase fluid: A homogenisation approach, *Transp. Porous Media*, *74*, 349–368.

Schanz, M. (2009), Poroelastodynamics: Linear models, analytical solutions, and numerical methods, *Appl. Mech. Rev.*, *62*, 030803, doi:10.1115/1.3090831.

Scheidegger, A. E. (1960), General theory of dispersion in porous media, *Appl. Mech. Rev.*, *13*, 313–318.

Selvadurai, A. P. S. (Ed.) (1996), *Mechanics of Poroelastic Media*, Kluwer Academic, Dordrecht, Netherlands.

Selvadurai, A. P. S. (2004), Stationary damage modelling of poroelastic contact, *Int. J. Solids Struct.*, *41*, 2043–2064.

Selvadurai, A. P. S. (2007), The analytical method in geomechanics, *Appl. Mech. Rev.*, *60*, 87–106.

Selvadurai, A. P. S., and A. Glowacki (2008), Permeability hysterisis of limestone during isotropic compression, *Ground Water*, *46*(1), 113–119.

Selvadurai, A. P. S., and P. A. Selvadurai (2010), Surface permeability tests: Experiments and modelling for estimating effective permeability, *Proc. R. Soc. A*, *466*, 2819–2846.

Selvadurai, A. P. S., and A. Shirazi (2005), An elliptical disc anchor in a damage-susceptible poroelastic medium, *Int. J. Numer. Methods Eng.*, *63*, 2017–2039.

Selvadurai, A. P. S., A. Letendre, and B. Hekimi (2011), Axial flow hydraulic pulse testing of an argillaceous limestone, *Environ. Earth Sci.*, *64*, 2047–2058.

Shao, J. F., D. Hoxha, M. Bart, F. Homand, G. Duveau, M. Souley, and N. Hoteit (1999), Modelling of induced anisotropic damage in granites, *Int. J. Rock Mech. Min. Sci.*, *36*, 1001–1012.

Sherwood, J. D. (1997), Packing of spheriods in three-dimensional space by random sequential addition, *J. Phys. A*, *30*, 839–843.

Shiping, L., L. Yushou, L. Yi, W. Zhenye, and Z. Gang (1994), Permeability-strain equations corresponding to the complete stress–strain path of Yinzhuang sandstone, *Int. J. Rock Mech. Min. Sci. Geomech. Abstr.*, *31*, 383–391.

Simpson, G. D. H., Y. Gueguen, and F. Schneider (2001), Permeability enhancement due to microcrack dilatancy in the damage regime, *J. Geophys. Res.*, *106*(B3), 3999–4016.

Smit, R. J. M., W. A. M. Brekelmans, and H. E. H. Meijer (1998), Prediction of the mechanical behaviour of nonlinear heterogeneous systems by multi-level finite element modeling, *Comp. Methods Appl. Mech. Eng.*, *155*, 181–192.

Souley, M., F. Homand, S. Pepa, and D. Hoxha (2001), Damage-induced permeability changes in granite: A case example at the URL in Canada, *Int. J. Rock Mech. Min. Sci.*, *38*, 297–310.

Stafford, D. S., and T. L. Jackson (2010), Using level sets for creating virtual random packs of non-spherical convex shapes, *J. Comp. Phys.*, *229*, 3295–3315.

Vasconcelos, G., P. B. Lourenço, C. A. S. Alves, and J. Pamplona (2008), Experimental characterisation of the tensile behaviour of granite, *Int. J. Rock Mech. Min. Sci.*, *45*, 268–277.

Vasconcelos G., P. B. Lourenço, C. A. S. Alves, and J. Pamplona (2009), Compressive behaviour of granite: Experimental approach, *J. Mater. Civil Eng.*, *21*(9), 502–511.

Wang, Y., and F. Tonon (2009), Modeling Lac du Bonnet granite using a discrete element model, *Int. J. Rock Mech. Min. Sci.*, *46*, 1124–1135.

Wells, G. N., and L. J. Sluys (2001), A new method for modelling cohesive cracks using finite elements, *Int. J. Numer. Methods Eng.*, *50*, 2667–2682.

Williams, S. R., and A. P. Philipse (2003), Random packings of spheres and spherocylinders simulated by mechanical contraction, *Phys. Rev. E*, *67*, 051301, doi:10.1103/PhysRevE.67.051301.

Yuan, S. C., and J. P. Harrison (2005), Development of a hydro-mechanical local degradation approach and its application to modelling fluid flow during progressive fracturing of heterogeneous rocks, *Int. J. Rock. Mech. Min. Sci.*, *42*, 961–984.

Zhang, H. W., and Z. D. Fu (2010), Coupling upscaling finite element method for consolidation analysis of heterogeneous saturated porous media, *Adv. Water Res.*, *33*, 34–47.

Zhou, J. J., J. F. Shao, and W. Y. Xu (2006), Coupled modeling of damage growth and permeability variation in brittle rocks, *Mech. Res. Commun.*, *33*, 450–459.

Zhu, W., L. G. J. Montesi, and T. F. Wong (2007), A probabilistic damage model of stress-induced permeability anisotropy during cataclastic flow, *J. Geophys. Res.*, *112*, B10207, doi:10.1029/2006JB004456.

Zhu, W., and T. F. Wong (1997), The transition from brittle faulting to cataclastic flow: Permeability evolution, *J. Geophys. Res.*, *102*, 3027–3041.

Zoback, M. D., and J. D. Byerlee (1975), The effect of microcrack dilatancy on the permeability of Westerly granite, *J. Geophys. Res.*, *80*, 752–755.